Journal of Coordination Chemistry

ISSN: (Print) (Online) Journal homepage: https://www.tandfonline.com/loi/gcoo20

Oxygenation of copper(I) complexes containing fluorine tagged tripodal tetradentate chelates: significant ligand electronic effects

Runzi Li, Firoz Shah Tuglak Khan, Marcos Tapia & Shabnam Hematian

To cite this article: Runzi Li, Firoz Shah Tuglak Khan, Marcos Tapia & Shabnam Hematian (2022) Oxygenation of copper(I) complexes containing fluorine tagged tripodal tetradentate chelates: significant ligand electronic effects, Journal of Coordination Chemistry, 75:11-14, 1617-1635, DOI: 10.1080/00958972.2022.2107429

To link to this article: https://doi.org/10.1080/00958972.2022.2107429

JOURNAL OF COORDINATION CHEMISTRY
2022, VOL. 75, NOS. 11–14, 1617–1635
https://doi.org/10.1080/00958972.2022.2107429

Oxygenation of copper(I) complexes containing fluorine tagged tripodal tetradentate chelates: significant ligand electronic effects

Runzi Li, Firoz Shah Tuglak Khan, Marcos Tapia and Shabnam Hematian

Department of Chemistry and Biochemistry, University of North Carolina at Greensboro, Greensboro, NC, USA

ABSTRACT

Copper-dioxygen (O_2) interactions are of great importance in biological and chemical transformations involving reversible dioxygen binding, activation, or reduction. In this report, we describe O_2-reactions with the mononuclear copper(I) complexes containing two new analogues of the known nitrogen-containing tetradentate tripodal chelate, *tris*[(2-pyridyl)methyl]amine (TMPA). In both derivatives, one electron-rich and one electron-deficient, fluorine atoms are attached to the ligand framework, allowing for the use of ^{19}F-NMR spectroscopy to probe the oxygenation process. Variations of ligand electronic properties are manifested in the electrochemical behavior of copper complexes and their reactivities toward O_2. Our NMR spectroscopic studies, along with variable-temperature electronic absorption measurements, revealed that the copper(I) complexes reversibly react with O_2 to form the corresponding 1:1 copper-O_2 (i.e., *end-on* superoxo) intermediates which can further react reversibly with second equivalents of copper(I) complexes to form the related dinuclear 2:1 copper-O_2 (i.e., *trans*-peroxo) adducts. However, considerable differences exist in detail at various temperatures, depending on the chelate. All three *end-on* superoxo and *trans*-peroxo species described here possess similar spectroscopic features, although small but significant shifts in the energy of their signature bands were observed, suggesting that the variation in the chelates directly affects the electronic properties of the copper-O_2 cores.

ARTICLE HISTORY
Received 19 April 2022
Accepted 14 July 2022

KEYWORDS
Copper; dioxygen; ligands; pyridines; substituents; fluorine; reactivity; intermediate; peroxide; superoxide

CONTACT Shabnam Hematian s_hemati@uncg.edu Department of Chemistry and Biochemistry, University of North Carolina at Greensboro, Greensboro, NC 27402, USA.

Supplemental data for this article is available online at https://doi.org/10.1080/00958972.2022.2107429.

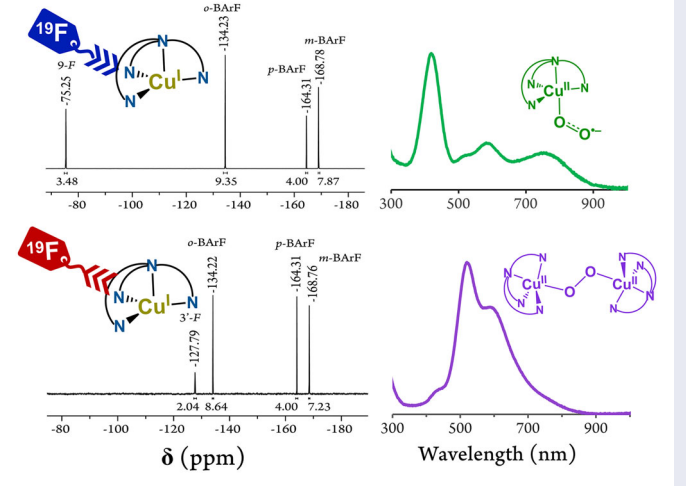

1. Introduction

The dioxygen (O_2) chemistry of synthetic copper(I) complexes and the oxidative properties of the resulting copper-O_2 adducts are of importance due to their potential relevance to copper-containing proteins vital for aerobic life as well as their applications in chemical catalysis [1–5]. In nature, copper-dioxygen interactions are essential for facilitating an array of biological functions in many proteins including the dioxygen-carrier hemocyanin, monooxygenases where O_2 is activated such as in tyrosinase, dopamine β-hydroxylase, and phenylalanine hydroxylase, or oxidases where O_2 is reduced to H_2O or H_2O_2 including in laccase, galactose oxidase, ascorbate oxidase, amine oxidase, and the heme-copper binuclear active site of cytochrome *c* oxidase [2,6–8].

One of the most well-studied synthetic systems that has provided particular insights into copper-O_2 chemistry is the mononuclear cuprous complex of the nitrogen-containing tetradentate tripodal ligand, *tris*[(2-pyridyl)methyl]amine (TMPA) [9–13]. The mononuclear complex $[(tmpa)Cu^{I}(MeCN)]^{+}$ reversibly binds O_2 to form an η^1 "*end-on*" cupric superoxide ($Cu^{II}-O_2^{\bullet-}$) species which then rapidly reacts, even at low temperatures, with another equivalent of cuprous complex to generate a binuclear *trans*-peroxo-dicopper(II) complex, $[(tmpa)Cu^{II}–(O_2)–Cu^{II}(tmpa)]^{2+}$ (Figure 1) [11,13–17].

Modifications of the TMPA framework to influence the steric and electronic properties of the donor atoms have shown that the presence of electron-donating substituents leads to energetic stabilization of the superoxo intermediate and chelates with large steric demands and a negative charge can prevent the dimerization and formation of the corresponding peroxo species in solution [10,13,18,19]. In this report, we describe and compare the oxygenation of the cuprous complexes of two new TMPA-derivatives, one electron-rich and one electron-deficient, with fluorine atoms attached to the chelate backbones which also provide the ability to probe the dioxygen reactivity of these systems through ^{19}F-NMR spectroscopy (Figure 2). The

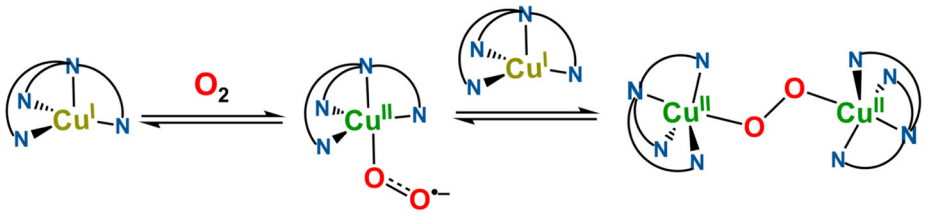

Figure 1. Mechanism for the oxygenation reaction of TMPA-like copper(I) complexes.

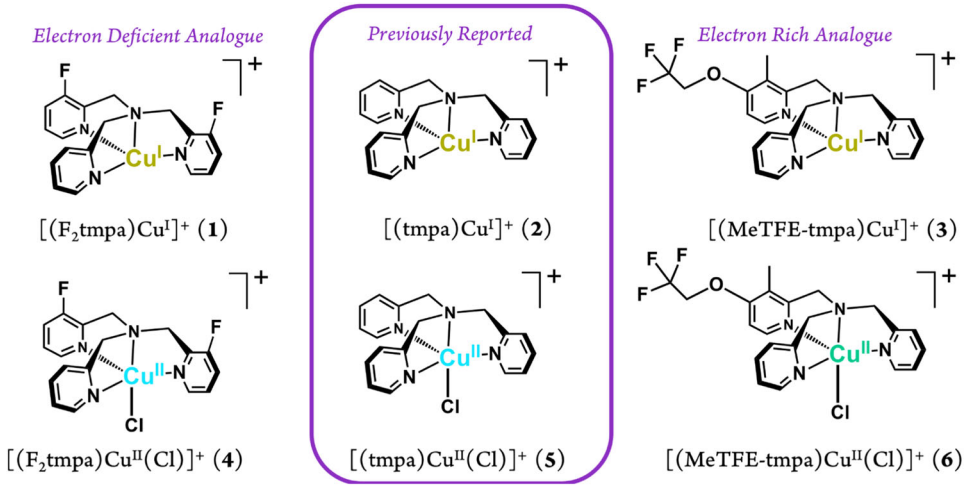

Figure 2. Copper(I) and copper(II) complexes described in this study. All complexes were prepared with $[B(C_6F_5)_4]^-$ as the counter anion.

dioxygen reactivities of the copper(I) complexes were investigated using ^{1}H- and ^{19}F-NMR spectroscopies along with variable-temperature UV-vis measurements. For comparison, the corresponding copper(II)-chloro complexes were also synthesized and characterized using a series of spectroscopic methods as well as cyclic voltammetry, mass spectrometry, and X-ray crystallography. The properties of copper(I) and copper(II)-chloro complexes are compared and contrasted, particularly with respect to the influence of the pyridyl substituents present in the new ligand scaffolds. Some mechanistic insights regarding oxygenation reactions are also presented.

2. Experimental

2.1. General methods

All chemicals were of commercially available grade and used without purification, unless noted otherwise. Acetonitrile (MeCN), dichloromethane (DCM), tetrahydrofuran

(THF), and 2-methyltetrahydrofuran (MeTHF) were purchased from Sigma-Aldrich. Methanol (MeOH) and diethyl ether were purchased from Fisher Chemical. Deuterated solvents ($CDCl_3$, CD_3CN, and THF-d_8) were purchased from Cambridge Isotope Laboratories. Commercial ACS grade solvents were used for chromatography and extractions. All solvents were purified by an Innovative Technologies or Inert PureSolv Micro solvent purification system prior to use for the reactions and characterizations. Solvents were then deoxygenated by bubbling with argon for 1 h followed by storage over 3 or 5 Å molecular sieves for at least 72 h prior to use. Deionized water was purified by a PURELAB flex 1 Analytical Ultrapure Water System (ELGA) to obtain nanopure water with a specific resistance of 18.2 MΩ cm at room temperature. Air- and moisture-sensitive compounds were prepared and handled under nitrogen in a Vacuum Atmospheres OMNI-Lab inert atmosphere (<0.5 ppm of O_2 and H_2O) glovebox, or under a dry, oxygen-free argon atmosphere using standard Schlenk techniques. Ultra-high purity grade oxygen gas was purchased from Airgas and passed through a drying column containing Drierite desiccant and 3 Å activated molecular sieves prior to use. For Nuclear Magnetic Resonance (NMR) experiments, dry O_2 gas was transferred and stored in a capped 50 mL Schlenk flask, then slowly bubbled into the metal complex solutions via a three-way long syringe needle.

Electrochemical data were collected using a Bio-Logic SP-200 potentiostat. UV-vis absorption spectra were recorded on a Cary-60 spectrophotometer equipped with a Unisoku CoolSpeK USP-203-B cryostat using 4 or 10 mm modified Schlenk quartz cuvettes. Infrared (IR) spectra of neat solid samples were obtained using a Thermo Scientific Nicolet iS5 Fourier Transform IR (FT-IR) spectrometer equipped with an iD7 attenuated total reflection (ATR) accessory. Proton and fluorine NMR spectra were recorded either on a JEOL 400 or 500 MHz spectrometer. For ^{1}H-NMR spectra, the chemical shifts were referenced against NMR solvent residual shifts (e.g., THF-d_8 at $\delta = 1.72$ ppm) and/or tetramethylsilane (TMS at $\delta = 0.00$ ppm). Electrospray ionization mass spectra (ESI-MS) of the ligands and copper complexes were collected in positive ion mode by a Waters Synapt G2 HDMS q-TOF system.

The compounds TMPA [17], [(tmpa)Cu^{II}(Cl)][$B(C_6F_5)_4$] (**5**) [20], and [(tmpa)Cu^{I}(MeCN)][$B(C_6F_5)_4$] [20] were prepared and characterized following methods previously described. [(tmpa)Cu^{I}(MeCN)][$B(C_6F_5)_4$] was further recrystallized from THF/hexanes affording [(tmpa)Cu^{I}][$B(C_6F_5)_4$] (**2**) and the absence of a bound MeCN ligand was confirmed through ^{1}H-NMR and FT-IR spectroscopies.

2.2. Synthesis and characterization of free ligands

2.2.1. F_2TMPA

Under continuous argon flow, a solution of picolylamine (0.96 mL, 9.2 mmol), 3-fluoro-2-formylpyridine (1.27 g, 10.1 mmol), and sodium triacetoxyborohydride (3.12 g, 14.72 mmol) in 1,2-dichloroethane (DCE; 40 mL) was stirred for 2 h. Additional 3-fluoro-2-formylpyridine (1.27 g, 10.1 mmol) and sodium triacetoxyborohydride (3.12 g, 14.72 mmol) were added and stirring was continued overnight. The reaction mixture was then mixed with 0.1 M aqueous HCl solution (60 mL; pH = 1), and the DCE layer was discarded. The aqueous layer was washed using DCM (2 × 20 mL), brought to pH

= 10 using NaOH pellets, then extracted using DCM (2 × 100 mL). The DCM fractions were evaporated under reduced pressure, redissolved in hot diethyl ether, then cooled at −20 °C overnight to obtain white crystals, which were washed with cold ether and dried under vacuum. Yield: 1.292 g (43%). ^{1}H-NMR (400 MHz, $CDCl_3$, δ, ppm): 8.46 (d, 1H), 8.35 (d, 2H), 7.57 (m, 2H), 7.31 (td, 2H), 7.19 (m, 2H), 7.09 (td, 1H), 4.03 (d, 2H), 3.99 (s, 1H) (supporting material Figure S1). ^{19}F-NMR (376 MHz, $CDCl_3$, δ, ppm): −123.38 (supporting material Figure S2). ESI-MS ($[F_2TMPA + H]^+$) calcd/found (*m/z*): 327.1421/327.1359 (supporting material Figure S3). FT-IR (solid): $\nu_{(C\text{-}H,\ Py\ and\ CH2)}$ = 3056, 3019, 2919, 2889, 2846, and 2819 cm^{-1} (supporting material Figure S4).

2.2.2. MeTFE-TMPA

An aqueous solution of 2-(chloromethyl)-3-methyl-4-(2,2,2-trifluoroethoxy)pyridine hydrochloride (6.74 g, 0.024 mol) was prepared, brought to pH = 10 using NaOH pellets, then extracted using DCM (2 × 100 mL). The DCM fractions were evaporated under reduced pressure, then redissolved in THF (80 mL) and transferred to a three-neck round-bottom flask under argon. Under continuous argon flow, the THF solution was stirred with di(2-picolyl)amine (4.9 g, 0.024 mol) and diisopropylamine (25.3 mL, 0.15 mol) for 1 week. After one week, the reaction mixture was evaporated under reduced pressure and purification was performed on an alumina column. The product fraction was eluted with 3–4% MeOH:DCM, evaporated under reduced pressure, redissolved in hot diethyl ether, then cooled at −20 °C overnight to obtain the light-brown solid product, which was washed with cold ether and dried under vacuum. Yield: 5.8081 g (59%). ^{1}H-NMR (400 MHz, $CDCl_3$, δ, ppm): 8.52 (d, 2H), 8.31 (d, 1H), 7.62 (td, 2H), 7.46 (d, 2H), 7.13 (td, 2H), 6.58 (d, 1H), 4.35 (q, 2H), 3.89 (s, 2H), 3.83 (s, 4H) (supporting material Figure S5). ^{19}F-NMR (376 MHz, $CDCl_3$, δ, ppm): −73.79 (supporting material Figure S6). ESI-MS ([MeTFE-TMPA + H]$^+$) calcd/found (*m/z*): 403.1746/403.1650 (supporting material Figure S7). FT-IR (solid): $\nu_{(C\text{-}H,\ Py\ and\ CH2)}$ = 3067, 3012, 2949, and 2824 cm^{-1} (supporting material Figure S4).

2.3. Synthesis and characterization of copper(I) complexes

2.3.1. $[(F_2tmpa)Cu^{I}][B(C_6F_5)_4]$ (1)

The complex was prepared following slight modification of the reported procedure for $[(tmpa)Cu^{I}][B(C_6F_5)_4]$ (**2**). In the glovebox, a solution of F_2TMPA (249.8 mg, 0.77 mmol) and $[Cu^{I}(MeCN)_4][B(C_6F_5)_4]$ (698.22 mg, 0.77 mmol) in THF (6 mL) was stirred for 30 min at room temperature. Hexane (40 mL) was added to precipitate the product as a yellow powder, then stirring was continued for 25 min. After allowing the mixture to sit for approximately 30 min to allow separation of the two layers, the hexane layer was decanted off as waste, and the hexane addition/decantation step was repeated twice more. The resulting THF solution was dried under vacuum to obtain the light-yellow solid product. Yield: 703.59 mg (86%). ^{1}H-NMR (500 MHz, CD_3CN, δ, ppm): 8.53 (s, 1H, 6-*H*), 8.41 (s, 2H, 6′-*H*), 7.79 (s, 1H, 4-*H*), 7.57 (s, 2H, 4′-*H*), 7.38 (m, 4H, 3-*H*, 5-*H*, 5′-*H*), 4.03 (s, 2H, -C*H*′$_2$-), 3.93 (s, 1H, -C*H*$_2$-) (supporting material Figure S8); (500 MHz, THF-d_8, δ, ppm): 8.75 (s, 3H, 6-*H*, 6′-*H*), 7.86 (s, 1H, 4-*H*), 7.72 (s, 2H, 4′-*H*), 7.57 (m, 4H, 3-*H*, 5-*H*, 5′-*H*), 4.63 (s, 3H, -C*H*′$_2$-, -C*H*$_2$-). ^{19}F-NMR (470 MHz, CD_3CN, δ, ppm): −127.8, −134.2,

–164.3, and –168.8 (supporting material Figure S9); (470 MHz, THF-d_8, δ, ppm): –123.9, –132.0, –164.3, and –167.8. ESI-MS ([(F_2tmpa)Cu^{I}]$^+$) calcd/found (*m/z*): 389.0639/389.0574 (supporting material Figure S10). FT-IR (solid): $\nu_{(C\text{-}H,\ Py\ and\ CH2)}$ = 3085, 2958, 2925, and 2862 cm^{-1} (supporting material Figure S11).

2.3.2. [(MeTFE-tmpa)Cu^{I}][$B(C_6F_5)_4$] (3)

The synthetic procedure was analogous to that of [(F_2tmpa)Cu^{I}][$B(C_6F_5)_4$], with MeTFE-TMPA (200.2 mg, 0.49 mmol) used in place of F_2TMPA. The product was obtained as a light-yellow solid. Yield: 483.8 mg (85%); ^{1}H-NMR (500 MHz, CD_3CN, δ, ppm): 8.52-8.36 (br s, 3H, 6-*H*, 6′-*H*), 7.80 (s, 2H, 4-*H*), 7.34 (br s, 4H, 3-*H*, 5-*H*), 6.94 (s, 1H, 5′-*H*), 4.58 (q, 2H, 8-*H*), 3.86 (s, 6H, -CH_2-), 2.07 (s, 3H, 7-H) (supporting material Figure S12); (500 MHz, THF-d_8, δ, ppm): 8.96 (br s, 3H, 6-*H*, 6′-*H*), 7.83 (s, 2H, 4-*H*), 7.53 (s, 4H, 3-*H*, 5-*H*), 7.20 (s, 1H, 5′-*H*), 4.73 (br s, 8H, 8-*H*, -CH_2-), 2.17 (s, 3H, 7-*H*). ^{19}F-NMR (470 MHz, CD_3CN, δ, ppm): –75.3, –134.2, –164.3, and –168.8 (supporting material Figure S13); (470 MHz, THF-d_8, δ, ppm): –74.5, –132.1, –164.3, and –167.8. ESI-MS ([(MeTFE-tmpa)Cu^{I}]$^+$) calcd/found (*m/z*): 465.0963/465.0890 (supporting material Figure S14). FT-IR (solid): $\nu_{(C\text{-}H,\ Py\ and\ CH2)}$ = 3069, 2961, 2872, and 2854 cm^{-1} (supporting material Figure S11).

2.4. Synthesis and characterization of copper(II) complexes

2.4.1. [(F_2tmpa)Cu^{II}(Cl)][$B(C_6F_5)_4$] (4)

The complex was prepared following slight modification of the reported procedure for [(tmpa)Cu^{II}(Cl)][$B(C_6F_5)_4$] (**5**) [20]. A clear green solution of $CuCl_2{\cdot}2H_2O$ (172.2 mg, 1.01 mmol), F_2TMPA (329.6 mg, 1.01 mmol), and 6 drops of water in MeCN (14 mL) was stirred for 10 min at room temperature. While continuing stirring, K[$B(C_6F_5)_4$] (725.3 mg, 1.01 mmol) was added to the reaction mixture, producing a white solid precipitate. The mixture was filtered to remove precipitated KCl, evaporated under reduced pressure, redissolved in diethyl ether (4 mL), and again evaporated under reduced pressure. The resulting solid was recrystallized by slowly cooling a hot MeOH/water solution to produce light blue-green crystals suitable for X-ray diffraction, which were then dried under vacuum. Yield: 881.2 mg (79%). UV-vis [λ_{max}, nm (ε_{max}, $M^{-1}cm^{-1}$)]: 310 (3,570), 734 (100), and 964 (205) in MeTHF (supporting material Figure S15). ^{1}H-NMR (500 MHz, CD_3CN, δ, ppm): 30.31 (br s, 3H, 5,5′-*H*), 10.84–10.04 (s, 3H, 4,4′-*H*) (supporting material Figure S16). ^{19}F-NMR (470 MHz, CD_3CN, δ, ppm): –106.19, –134.2, –164.3, and –168.8 (supporting material Figure S17). ESI-MS ([(F_2tmpa)Cu^{II}(Cl)]$^+$) calcd/found (*m/z*): 424.0328/424.0192 (supporting material Figure S18). FT-IR (solid): $\nu_{(C\text{-}H,\ Py\ and\ CH2)}$ = 3127, 3101, 3088, and 3082 cm^{-1} (supporting material Figure S19).

2.4.2. [(MeTFE-tmpa)Cu^{II}(Cl)][$B(C_6F_5)_4$] (6)

The synthetic procedure was analogous to that of **4**, with MeTFE-TMPA used in place of F_2TMPA. The product was obtained as a light-green microcrystalline solid. Yield: 908.7 mg (77%) UV-vis [λ_{max}, nm (ε_{max}, $M^{-1}cm^{-1}$)]: 302 (3750), 734 (98), and 964 (218) in MeTHF (supporting material Figure S15). ^{1}H-NMR (500 MHz, CD_3CN, δ, ppm): 22.94 (br s, 5H, 3,5,5′-*H*), 10.48 (s, 2H, 4-*H*), 4.67 (s, 2H, 8-*H*) (supporting material Figure S20).

^{19}F-NMR (470 MHz, CD_3 CN, δ, ppm): −75.02, −134.2, −164.3, and −168.8 (supporting material Figure S21). ESI-MS ([(MeTFE-tmpa)Cu^{II}(Cl)]$^+$) calcd/found (*m/z*): 500.0652/500.0555 (supporting material Figure S22). FT-IR (solid): $\nu_{(C\text{-}H,\ Py\ and\ CH2)}$ = 3110, 3076, 2952, and 2924 cm^{-1} (supporting material Figure S19).

2.5. Single-crystal X-ray diffraction

Suitable X-ray quality single crystals of [(F_2tmpa)Cu^{II}(Cl)][$B(C_6F_5)_4$] were obtained by recrystallization in hot MeOH/water. All reflection intensities were measured at 100(2) K using a Gemini R diffractometer (equipped with an Atlas detector) with Mo-Kα radiation ($\lambda = 0.71073$ Å) under the program CrysAlisPro (Version CrysAlisPro 1.171.38.43f, Rigaku OD, 2015). The same program (but a different version viz. CrysAlisPro 1.171.40.53, Rigaku OD, 2019) was used to refine the cell dimensions and for data reduction. The temperature of the data collection was controlled using the system Cryojet (manufactured by Oxford Instruments, Abingdon, UK). The structure was solved with the program SHELXT-2018/2 and was refined on F^2 by full-matrix least-squares using the SHELXL-2018/3 program package [21]. Numerical absorption correction based on Gaussian integration was applied using a multifaceted crystal model by CrysAlisPro. Non-hydrogen atoms were refined anisotropically. In the refinement, hydrogen atoms were treated as riding atoms using SHELXL default parameters. The SUMP command in SHELXL was used to fix the occupancy factors of the fluorine atoms on pyridyl ring to two.

The Cambridge Crystallographic Data Center (CCDC no. 2163521) contains the supplementary crystallographic data for this article. The data can be obtained free of charge via https://www.ccdc.cam.ac.uk/data_request/cif.

2.6. Electrochemical studies

Electrochemical data were collected under nitrogen in the glovebox using a three-electrode cell. A leak-free Ag/AgCl reference electrode (Innovative Instruments, Inc.), a 3.0-mm glassy carbon working electrode, and a graphite carbon rod counter electrode were used for the measurements. The electrodes were cleaned using nanopure water and acetone prior to each experiment. The supporting electrolyte solution was 100 mM of [(nBu)$_4$N][PF_6] in MeCN. The sample solutions (2 mM analyte, 100 mM electrolyte) were scanned anodically then cathodically at varying scan rates (25, 50, 100, 250, 500, 750, and 1000 $mV{\cdot}s^{-1}$; supporting material Figures S23–S28 and supporting material Table S1). All potentials were further confirmed with the ferricenium/ferrocene couple ($E_{1/2}$ = 0.450 V *vs.* Ag/AgCl under identical conditions) as an internal reference [22].

2.7. Dioxygen reactivity studies

2.7.1. Room temperature UV-vis absorption studies

The general procedure for dioxygen reactivities of the [(L)Cu^{I}][$B(C_6F_5)_4$] complexes (L: F_2TMPA, TMPA, or MeTFE-TMPA) is described below, with L being TMPA as a

representative case. A stock solution of 5.4 mg (0.005 mmol) of [(tmpa)Cu^{I}][$B(C_6F_5)_4$] in MeTHF (2 mL) was prepared inside the glovebox. Samples for UV-vis measurements (450 μM concentration) were prepared by diluting 180 μL of this stock solution with MeTHF to 1 mL, then transferred to a 4-mm modified Schlenk cuvette equipped with a septum. UV-vis spectra were recorded upon the bubbling of dry O_2 gas directly into the solution at room temperature.

2.7.2. Low-temperature UV-vis absorption studies

The general procedure for the dioxygen reactivities of the [(L)Cu^{I}][$B(C_6F_5)_4$] complexes (L: F_2TMPA, TMPA, or MeTFE-TMPA) is described below, with L being MeTFE-TMPA as a representative case. A stock solution of 6.9 mg (0.006 mmol) of [(MeTFE-tmpa)Cu^{I}][$B(C_6F_5)_4$] in MeTHF (2 mL) was prepared inside the glovebox. Samples for UV-vis measurements (450 μM concentration) were prepared by diluting 180 μL of this stock solution with MeTHF to 1 mL, then transferred to a 4-mm modified Schlenk cuvette equipped with a septum. UV-vis spectra were recorded upon the bubbling of dry O_2 gas directly into the solution at −80 or −110 °C. The solution was monitored at −80 or −110 °C for 30 min after O_2 bubbling, then allowed to warm to room temperature. The solution was further monitored for 1 h 30 min, with spectra recorded at −80 or −110 °C.

2.7.3. Nuclear magnetic resonance (NMR) studies

The experimental details were similar to our recently reported procedure for the dioxygen reactivity of [(tmpa)Cu^{I}(MeCN)][$B(C_6F_5)_4$] [23]. Details are given for [(F_2tmpa)Cu^{I}][$B(C_6F_5)_4$] as a representative case for the O_2-reactivity of the copper(I) complexes in this study. Inside the glovebox, a solution of [(F_2tmpa)Cu^{I}][$B(C_6F_5)_4$] (29.4 mg, 0.028 mmol) was dissolved in THF-d_8 (800 μL) and transferred to an NMR tube. The sample was sealed with a rubber septum and transferred outside, and its spectrum was recorded at room temperature. For oxygenation, 4 mL of dry O_2 gas was slowly bubbled into the sample solution using a Hamilton gastight syringe equipped with a three-way valve. After O_2 bubbling, the first spectrum was recorded within 2 min of mixing, and the reaction was monitored over 6 h.

3. Results and discussion

3.1. Structural and physical properties of copper complexes

3.1.1. New ligands

To study the electronic effects in modulating the dioxygen reactivity of the cuprous complexes, we prepared two new TMPA-based ligands, with either electron-withdrawing or -donating groups on the pyridyl arms. Inclusion of fluorine groups on the backbone of the chelates also provided an additional tool for probing the oxygenation reactions. In the electron-deficient F_2TMPA chelate, fluorine atoms occupy the 3′-position of the two substituted pyridyl rings whereas in the electron-rich MeTFE-TMPA derivative, a methyl group along with a trifluoroethoxy (TFE) pendant are attached to the 3′ and 4′-positions of the substituted pyridyl ring, respectively. From the coordination chemistry perspective, the ligands were designed such that in both TMPA derivatives, two of the three pyridyl rings serve as weaker σ-donors as compared to the third pyridyl arm (i.e., the two fluorine-substituted pyridine rings in F_2TMPA relative to

its unsubstituted arm, or the two unsubstituted pyridine rings in MeTFE-TMPA compared to the 3-methyl-4-(2,2,2-trifluoroethoxy)pyridine arm). The ligand F_2TMPA was synthesized through reductive amination while MeTFE-TMPA was prepared via a nucleophilic substitution reaction. Further details are presented in the Experimental section and supporting material Scheme S1. Both tetradentate ligands contain groups with fluorine atoms which can be probed using ^{19}F-NMR spectroscopy. Both ligands were characterized through ^{1}H- and ^{19}F-NMR, FT-IR, and ESI-MS measurements. It is important to note that previously, synthetic difficulties were described as the reason for not including any O_2-reactivity studies of the TMPA-based cuprous complexes with electron-withdrawing groups [24].

3.1.2. Copper(I) complexes

Cuprous complexes were synthesized with *tetrakis*(pentafluorophenyl)borate, $[B(C_6F_5)_4]^-$, as a counter anion for enhanced solubility, by mixing one equivalent of each ligand and $[Cu^{I}(MeCN)_4][B(C_6F_5)_4]$ in THF in the glovebox (see Experimental section). Previous reports have shown that copper(I) complexes of TMPA-like ligands effect reductive dehalogenation reactions with a wide range of organohalide substrates [25–28]. Even a reactivity study of a TMPA-based chelate possessing a pendant R–Cl moiety (i.e., internal substrate) revealed the involvement of a copper-alkyl intermediate [29]. However, regarding the MeTFE-TMPA ligand, the presence of the trifluoroethoxy arm on the 4′-pyridyl position during the preparation of the copper(I) complex led to no observable reductive defluorination reaction, likely due to the stronger carbon-fluorine bonds as compared to those of other halides.

Both cuprous complexes, $[(F_2tmpa)Cu^{I}][B(C_6F_5)_4]$ and $[(MeTFE\text{-}tmpa)Cu^{I}][B(C_6F_5)_4]$, were characterized using UV-vis, FT-IR, ^{1}H- and ^{19}F-NMR spectroscopies as well as mass spectrometry and cyclic voltammetry. The ^{19}F-NMR spectra of the two cuprous complexes supported the presence of one equivalent of $[B(C_6F_5)_4]^-$ per ligand-copper moiety. Moreover, the parent $[(tmpa)Cu^{I}(MeCN)]^+$ possesses one coordinated acetonitrile molecule per tetradentate ligand-copper core, preferring five-coordinate geometry while the bound MeCN ligand can be removed by multiple recrystallization from a weakly coordinating solvent such as THF or diethyl ether [25,28]. The ^{1}H-NMR and IR spectra of the two new isolated copper(I) complexes with F_2TMPA and MeTFE-TMPA revealed that both systems adopt a four-coordinate formulation $[(L)Cu^{I}]^+$ with no MeCN incorporated as a fifth ligand. This is not surprising as these complexes were prepared and isolated in THF.

3.1.3. Copper(II) complexes

The copper(II)-chloro complexes of the two new chelates, F_2TMPA and MeTFE-TMPA, were prepared following a similar procedure to the one previously reported for the parent complex, $[(tmpa)Cu^{II}(Cl)][B(C_6F_5)_4]$ [20]. The ^{19}F-NMR spectra of the copper(II)-chloro complexes, with F_2TMPA or MeTFE-TMPA, confirmed the association of one equivalent of $[B(C_6F_5)_4]^-$ with one ligand-copper moiety in each system. The complexation of copper(II)-chloro complexes was further confirmed via ^{1}H-NMR, FT-IR, mass spectrometry, and cyclic voltammetry measurements. The reduction potentials of the copper(II)-chloro complexes are significantly lower ($>$340 mV) than those of the cuprous complexes (vide infra).

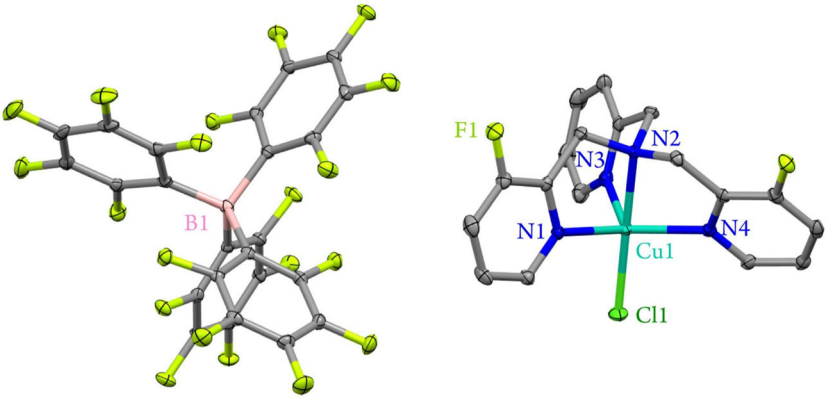

Figure 3. Displacement ellipsoid plot (50% probability level) of $[(F_2tmpa)Cu^{II}(Cl)][B(C_6F_5)_4]$, showing the atom-labeling scheme. Hydrogen atoms have been omitted for the sake of clarity. Selected bond lengths (Å) and angles (deg): Cu(1)-N(1), 2.0596(15); Cu(1)-N(2), 2.0553(14); Cu(1)-N(3), 2.1016(15); Cu(1)-N(4), 2.0400(15); Cu(1)-Cl(1), 2.2311(5); N(4)-Cu(1)-N(2), 80.29(6); N(4)-Cu(1)-N(1), 131.10(6); N(2)-Cu(1)-N(1), 81.24(6); N(4)-Cu(1)-N(3), 112.45(6); N(2)-Cu(1)-N(3), 80.55(6); N(1)-Cu(1)-N(3), 108.51(6); N(4)-Cu(1)-Cl(1), 98.83(4); N(2)-Cu(1)-Cl(1), 178.19(4); N(1)-Cu(1)-Cl(1), 98.24(4); N(3)-Cu(1)-Cl(1), 101.25(4).

In contrast to the four-coordinate structures of $[(L)Cu^{I}][B(C_6F_5)_4]$ (L: F_2TMPA, TMPA, and MeTFE-TMPA) but common in copper(I) ion chemistry, the copper centers in the copper(II)-chloro counterparts are five-coordinate. In general, a complex with a five-coordinate cupric center in a square pyramidal (*SP*) environment exhibits a broad band in the visible region (590–780 nm) along with a low-energy spin-forbidden shoulder at $\lambda > 800$ nm, whereas in a trigonal bipyramidal (*TBP*) geometry, the complex displays a main d-d transition at $\lambda > 800$ nm with a high-energy shoulder in the visible region [30]. The electronic absorption spectra of the parent as well as the two new copper(II)-chloro complexes exhibit one main d-d transition band centered at 964 nm and a shoulder at 734 nm, revealing that the *TBP* geometry is dominant is all three cupric systems in solution (supporting material Figure S15).

The intense ligand-to-metal charge transfer (LMCT) bands from the bound chloride ligand to the cupric center in the complexes bearing the F_2TMPA, TMPA, and MeTFE-TMPA chelates appear at 310, 305, and 302 nm, respectively, supporting the more stabilized d_{z2} orbitals in the former, $[(F_2tmpa)Cu^{II}(Cl)][B(C_6F_5)_4]$.

3.1.4. Crystal structure of $[(F_2tmpa)Cu^{II}(Cl)][B(C_6F_5)_4]$

The complex crystallizes in a triclinic crystal system with *P*-1 space group (see Experimental section, supporting material Figure S29 and Table S2). The molecular structure of the complex is shown in Figure 3 and relevant bond distances and angles are given in the figure captions. The cupric center is five-coordinate with three pyridyl nitrogens (N1, N3, and N4) and one tertiary alkyl amino nitrogen (N2) along with a chloride.

The Addison-Reedijk geometry analysis allows for the semiquantitative estimation of the prevalent geometry in crystalline phase [31], further supporting that the cupric center adjusts to a distorted *TBP* ($\tau_5 = 0.78$) coordination environment in F_2TMPA while the ligation in the parent TMPA analogue is reported to occur within a nearly

Table 1. $E_{1/2}$ and ΔE_p[a] values of copper complexes (2 mM) described in this study in MeCN with $[(n\text{Bu})_4\text{N}][\text{PF}_6]$ (100 mM) as the supporting electrolyte.

Complex	$E_{1/2}$ *vs.* Ag/AgCl (V)	$E_{1/2}$ *vs.* Fc/Fc^+ (V)	ΔE_p (mV)[a]	i_{pa}/i_{pc}
$[(F_2\text{tmpa})Cu^{I}][B(C_6F_5)_4]$	+0.150	−0.300	105	0.955
$[(\text{tmpa})Cu^{I}][B(C_6F_5)_4]$	+0.038	−0.412	94	0.941
$[(\text{MeTFE-tmpa})Cu^{I}][B(C_6F_5)_4]$	−0.010	−0.460	112	0.944
$[(F_2\text{tmpa})Cu^{II}(Cl)][B(C_6F_5)_4]$	−0.213	−0.663	95	0.861
$[(\text{tmpa})Cu^{II}(Cl)][B(C_6F_5)_4]$	−0.306	−0.756	100	0.786
$[(\text{MeTFE-tmpa})Cu^{II}(Cl)][B(C_6F_5)_4]$	−0.348	−0.798	107	0.955

[a]The values were obtained at 100 mV s^{-1} scan rate.

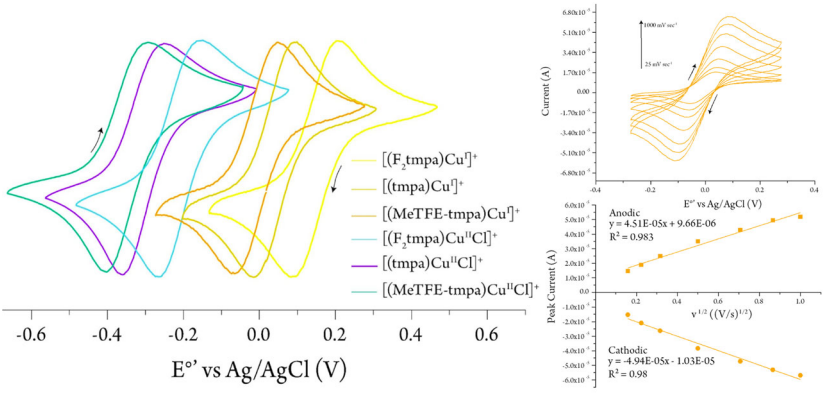

Figure 4. Electrochemical data obtained for copper complexes described in this study. (Left) Normalized cyclic voltammograms of **1**–**6** at 100 mV·s^{-1} scan rate. (Right) Representative cyclic voltammograms of $[(\text{MeTFE-tmpa})Cu^{I}][B(C_6F_5)_4]$ (2 mM) at various scan rates along with the Randles–Sevcik plot of the CV data. All measurements were performed in MeCN with 100 mM of $[(n\text{Bu})_4\text{N}][\text{PF}_6]$ as the supporting electrolyte.

perfect *TBP* geometry ($\tau_5 = 0.95$) [20]. The prominent *TBP* organization of the ligands around the cupric center observed in the crystalline phase agrees well with those speculated from their d-d absorption patterns for the solution phase (vide supra).

3.1.5. Electrochemistry

The electrochemical behavior of the copper complexes was studied by cyclic voltammetry (CV) under an inert atmosphere in MeCN. The data are given in Table 1. All complexes display a single one-electron transfer process showing quasireversible behavior with peak-to-peak separation values, ΔE_p, no more than 112 mV (Table 1) and anodic/cathodic peak current ratios (i_{pa}/i_{pc}) between 0.96 and 0.79.

Our Randles-Sevcik analysis of the peak current *vs.* the square root of the scan rate confirmed that in all cases, the species involved in the redox reactions were freely diffusing through the solution. The diffusion coefficients (D) of the cupric and cuprous forms of the $[(L)Cu]^{n+}$ species are between 1.39 and 3.65×10^{-6} cm^2 s^{-1} (supporting material Table S1). It is worth noting that the presence of the chloride ligand systematically decreases the reduction potential of the copper center by about 350 mV in all three chelate environments (Figure 4). The reversibility of the voltammograms of the copper(II)-chloro complexes, even at slower scan rates (e.g., 25 mV·s^{-1}), and the absence of any additional irreversible anodic peaks associated with the free copper

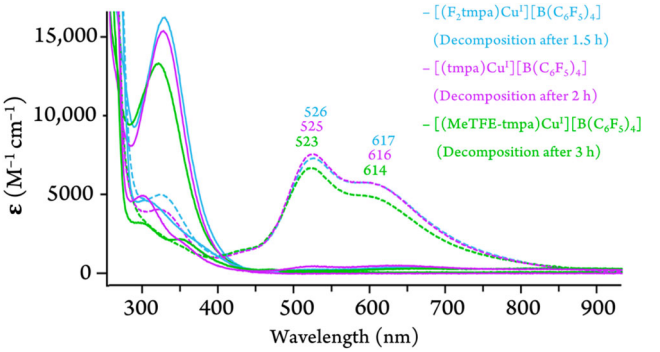

Figure 5. Room temperature UV-vis spectra of MeTHF solutions of the copper(I) complexes before O_2 addition (solid lines), immediately after 5 s of O_2 bubbling (dotted lines), and after ~100% decomposition. *Note:* The molar extinction coefficients are shown per two copper centers forming the *trans*-peroxo-dicopper(II) species (i.e., the ε values for the monomer cuprous complexes are in the range of 6-8 $mM^{-1}cm^{-1}$).

chelates also confirm that the axial chloride remains bound to the copper center during the reduction event.

The data shown for copper complexes reveal that, with substituted pyridyl ligands bearing electron-donating or -withdrawing groups, the $E_{1/2}$ value for the $Cu^{II/I}$ redox couple becomes more negative or more positive compared to that for the complex with the parent TMPA ligand, respectively. In other words, MeTFE-TMPA scaffold results in a more thermodynamically stable copper(II) complex while F_2TMPA forms a more thermodynamically stable copper(I) species as compared to the parent system. The variation in electrochemical behavior of copper(I) species with pyridyl ligands correlates to the O_2-reactivity differences observed in these systems (vide infra).

3.2. Oxygenation reactions of copper(I) complexes

The interaction of cuprous complexes, $[(L)Cu^{I}][B(C_6F_5)_4]$ (L: F_2TMPA, TMPA, and MeTFE-TMPA), with dioxygen in MeTHF follows the same basic mechanism which has been reported for other TMPA-like systems as described in the Introduction (Figure 1). The oxygenation reactions were monitored by variable temperature electronic absorption as well as ^{1}H- and ^{19}F-NMR spectroscopies.

3.2.1. UV-vis absorption spectroscopy

Bubbling O_2 into the solution of each copper(I) complex at room temperature resulted in the signature, intense color change from light yellow to purple known for formation of binuclear *trans*-peroxo-dicopper(II) complexes (Figure 5) [13,14,32]. The absorption spectra of the purple *trans*-peroxo-dicopper(II) intermediates with the F_2TMPA, TMPA, and MeTFE-TMPA chelates in MeTHF solution showed intense absorption bands at 526, 525, and 523 nm along with shoulders at 617, 616, and 614 nm, respectively. These two characteristic spectral features in the visible region are respectively ascribed to $\pi_\sigma^* \rightarrow d$ and $\pi_v^* \rightarrow d$ charge transfer (CT) transitions from the *trans*-peroxo ligand to the two copper centers and are consistent with the presence of highly covalent Cu–O bonds [7,33,34].

Close analysis of the previously reported X-ray structure of the parent *trans*-peroxo species, $[(tmpa)Cu^{II}–(O_2)–Cu^{II}(tmpa)]^{2+}$, reveals that the copper centers display an almost ideal *TBP* geometry ($\tau_5 = 0.89$), consistent with the structure of its copper(II)-chloro analogue, $[(tmpa)Cu^{II}(Cl)]^{+}$ ($\tau_5 = 0.95$). Assuming the same relationship exists between the two new *trans*-peroxo-dicopper(II) complexes and the corresponding copper(II)-chloro counterparts, the τ_5 value and supporting electronic absorption results would suggest that the cupric site of the corresponding *trans*-peroxo species, though to different degrees, adjust to a distorted *TBP* coordination environment, thus, supporting a d_{z2} ground state. The systematic hypsochromic (i.e., blue) shift of both CT bands in moving from the electron-deficient system bearing F_2TMPA to the electron-rich analogue with MeTFE-TMPA strongly suggests that the higher degree of electron donation from the chelate destabilizes d_{z2}, hence, shifting the LMCT bands from the bridging peroxide π^*-orbitals to the cupric center to higher energies (i.e., hypsochromic shift).

Interestingly, the spectra recorded immediately after the addition of O_2 to the three cuprous solutions revealed that the electron-rich $[(MeTFE\text{-}tmpa)Cu^{I}][B(C_6F_5)_4]$ (**3**) system instantaneously reacted with O_2 with no residual amount of cuprous species left while in the case of the parent $[(tmpa)Cu^{I}][B(C_6F_5)_4]$ (**2**) complex and its electron-deficient derivative, $[(F_2tmpa)Cu^{I}][B(C_6F_5)_4]$ (**1**), some cuprous species were still present in the solution. The observed trend follows the redox potential pattern of the cuprous complexes. Thus, the thermodynamic stability of the *trans*-peroxo species bearing MeTFE-TMPA is much higher than that of the TMPA or F_2TMPA analogues manifesting a considerable ligand electronic effect. This finding is in agreement with our NMR studies at room temperature, confirming that the *trans*-peroxo species of MeTFE-TMPA is significantly more stable than its more electron-deficient analogues (vide infra).

The association of two cuprous complexes with O_2 to form a *trans*-peroxo bridged dicopper assembly is an entropically unfavorable process, but the effect of this entropic cost can be alleviated by lowering the temperature. Lower temperatures also increase the lifetime of the initially formed copper-dioxygen intermediates not only by reducing the entropic costs of formation, but also by attenuating subsequent reactions. Therefore, further investigation of the oxygenation reactions of the copper(I) complexes were performed at lower reaction temperatures. At –80 °C, the copper(I) complexes of TMPA and F_2TMPA instantly reacted with dioxygen to form the corresponding *trans*-peroxo dicopper (i.e., 2:1 copper-dioxygen) intermediates with no sign of residual cuprous complex (Figure 6). The resulting *trans*-peroxo species were stable at –80 °C and only decomposed upon briefly warming to room temperature. While no *end-on* superoxo (i.e., 1:1 copper-dioxygen) intermediates were detected within the measurement time (i.e., 5 s) during the oxygenation of either copper(I)-TMPA or -F_2TMPA complex, a significant amount of this transient species was observed from the reaction of O_2 with the copper(I)-MeTFE-TMPA complex with λ_{max} at 425 nm and 765 nm, which within 30 min of O_2 bubbling, fully converted into the stable *trans*-peroxo complex, $[(MeTFE\text{-}tmpa)Cu^{II}–(O_2)–Cu^{II}(MeTFE\text{-}tmpa)]^{2+}$, with λ_{max} at 518 nm and 600 nm.

Further lowering the temperature to –110 °C led to remarkable differences in the oxygenation reactivities compared to those at –80 °C as is evident in Figures 6 and 7. The addition of O_2 to all three copper(I) complexes at –110 °C in MeTHF instantly led to full formation of the corresponding *end-on* superoxo intermediates. In the case of MeTFE-TMPA, a clean and stable *end-on* superoxo species was formed with an intense

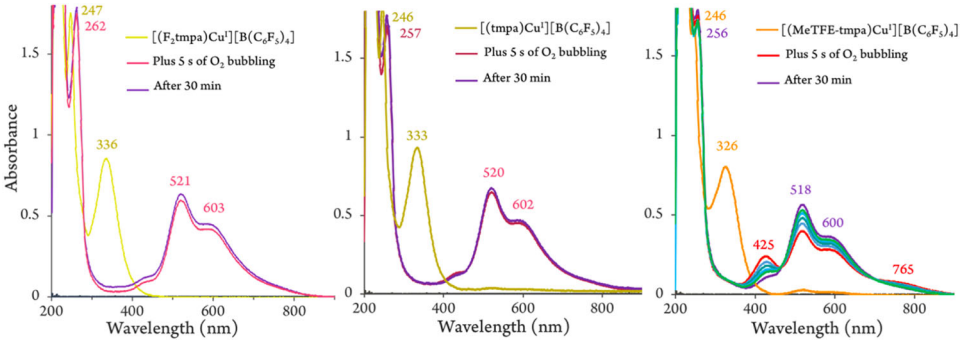

Figure 6. UV-vis spectral changes observed during reaction of the copper(I) complexes with O_2 in MeTHF at –80 °C.

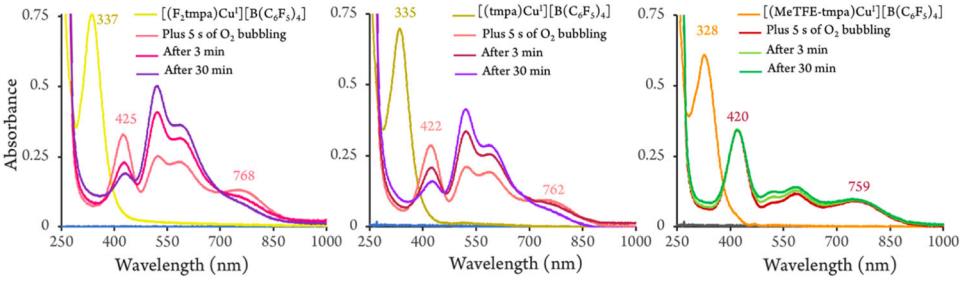

Figure 7. UV-vis spectral changes observed during reaction of the copper(I) complexes with O_2 in MeTHF at –110 °C.

absorption band at 420 nm, two weaker features at 519 and 587 nm, and a more prominent band at 759 nm. The former has been tentatively assigned to a $\pi_\sigma^* \rightarrow d$ CT transition, in which the in-plane π_σ^* orbital of the superoxide ion overlaps in σ fashion, with the d_{z2} orbital of the cupric center [13]. The oxygenation of the other two copper(I) complexes, **1** and **2**, however, resulted in the formation of a mixture of the corresponding 1:1 and 2:1 copper-O_2 adducts, with the *end-on* superoxo intermediate initially being the major species and readily converting to the corresponding *trans*-peroxo dicopper complex.

Comparisons of copper(I)-dioxygen reactivities at different temperatures point to varying degrees of change in the rate of initial reversible O_2 binding and the subsequent formation of the bridged *trans*-peroxo complex. At –80 °C, much slower transformation of the *end-on* superoxo into the *trans*-peroxo species with the MeTFE-TMPA chelate as compared to the other two systems suggests that the concentration of the copper(I) complex, **3**, must be minute due to a very large equilibrium constant for formation of the *end-on* superoxo complex at that temperature. These results are indicative of a clear ligand electronic effect, precluding formation of the corresponding *trans*-peroxo at the lowest temperature, –110 °C. At higher temperatures, the rate of formation of the *trans*-peroxo complex bearing MeTFE-TMPA strongly increases as is particularly noticeable in comparing Figures 5–7. This is again likely due to the shift in the equilibrium between **3** and the corresponding *end-on* superoxo species, making **3** available for the formation of the peroxo complex.

Table 2. Major electronic absorption features of the cupric *end-on* superoxo at −110 °C[a] and *trans*-peroxo complexes at room temperature.[b]

Dioxygen adduct	λ_{max} (nm)
$[(F_2tmpa)Cu^{II}\text{-}(O_2^{\cdot-})]^+$	425 and 768[a]
$[(tmpa)Cu^{II}\text{-}(O_2^{\cdot-})]^+$	422 and 762[a]
$[(MeTFE\text{-}tmpa)Cu^{II}\text{-}(O_2^{\cdot-})]^+$	420 and 759[a]
$[(F_2tmpa)Cu^{II}\text{–}(O_2^{2-})\text{–}Cu^{II}(F_2tmpa)]^{2+}$	526 and 617[b]
$[(tmpa)Cu^{II}\text{–}(O_2^{2-})\text{–}Cu^{II}(tmpa)]^{2+}$	525 and 616[b]
$[(MeTFE\text{-}tmpa)Cu^{II}\text{–}(O_2^{2-})\text{–}Cu^{II}(MeTFE\text{-}tmpa)]^{2+}$	523 and 614[b]

We also note that a similar correlation between the electronic effects of the three chelates and the energy of the absorption features in both *end-on* superoxo and *trans*-peroxo dicopper species were observed. As listed in Table 2, all CT bands shift to lower energies as the chelates become more electron-deficient and stabilize the d_{z2} orbitals.

3.2.2. Nuclear magnetic resonance spectroscopy

To further confirm the formation of *trans*-peroxo-dicopper(II) species and subsequent decomposition as observed in the UV-vis studies (vide supra), the dioxygen reactivity of the cuprous complexes was studied through ^{1}H- and ^{19}F-NMR spectroscopies at room temperature. Karlin and co-workers have previously shown that the two cupric centers in the parent *trans*-peroxo-dicopper(II) assembly were strongly antiferromagnetically coupled (i.e., singlet ground state) [25], therefore, well resolved ligand resonances in both ^{1}H- and ^{19}F-NMR spectra were expected.

The ^{1}H-NMR spectrum of $[(F_2tmpa)Cu^{I}][B(C_6F_5)_4]$ (**1**) in THF-d_8 displayed four signals between $\delta = 8.75$–7.57 ppm corresponding to protons of the pyridyl arms, while the methylene protons appeared at $\delta = 4.63$ ppm (Figure 8). The addition of dry O_2 and the subsequent formation of the *trans*-peroxo-dicopper(II) species resulted in a downfield shift of the proton resonances (i.e., $\delta_{Py\text{-}H} = 10.83$, 8.24, 7.95, and 7.76 ppm and $\delta_{\text{-}CH2} = 5.77$ ppm), reflecting the expected deshielding that was associated with the removal of electron density from the copper center. A similar trend was also observed in the ^{1}H-NMR spectra for oxygenation of the parent system with the TMPA chelate, in THF-d_8 (supporting material Figures S30 and S31) [23], consistent with the reactivity pattern previously reported in CD_2Cl_2 [25].

Due to decomposition of the *trans*-peroxo-dicopper(II) intermediates to paramagnetic monomeric copper(II) species, different and growing amounts of these final decomposition products were present throughout the oxygenation reactions of all the cuprous systems. In general, ^{1}H-NMR signals of mononuclear copper(II) complexes are either not observed or very broad due to the relatively long electronic relaxation time (i.e., $\tau_s \approx 10^{-9}$ s for Cu^{2+}), which leads to line broadening [35,36]. For instance, the initial spectrum for the dioxygen-exposed solution of $[(F_2tmpa)Cu^{I}][B(C_6F_5)_4]$ showed additional broad peaks at $\delta = 10.66$ and 9.54 ppm along with a series of paramagnetic signals in the downfield region ($\delta = 16.42$–43.56 ppm) which all corresponded to the monomeric $[(F_2tmpa)Cu^{II}(X)]^{n+}$ species [35]. Decomposition of the *trans*-peroxo-dicopper(II) intermediates to the final monomeric cupric products were completed within a few hours at room temperature.

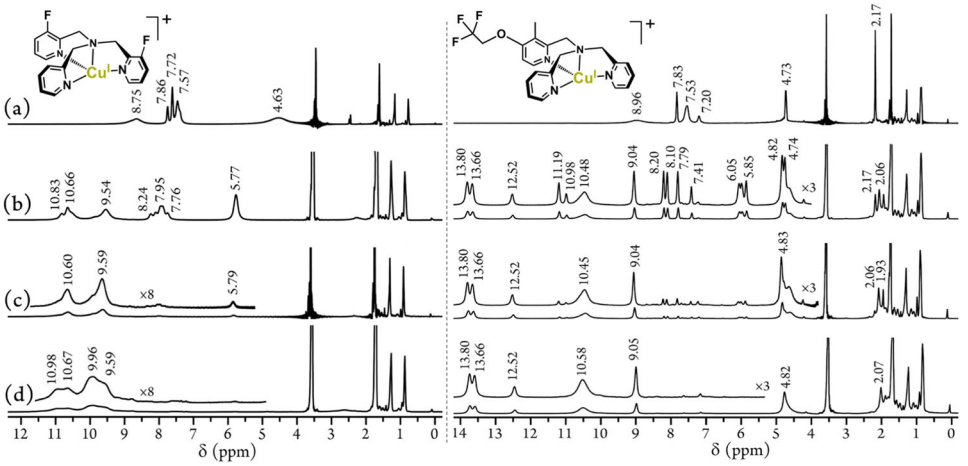

Figure 8. Diamagnetic region of the ^{1}H-NMR spectra of the oxygenation reactions of (left) [(F_2tmpa)Cu^{I}][$B(C_6F_5)_4$] and (right) [(MeTFE-tmpa)Cu^{I}][$B(C_6F_5)_4$] at (a) 0 min, (b) 1 min, (c) 15 min, and (d) 6 h in THF-d_8 (500 MHz) at room temperature.

The dioxygen reactivity of **1** was also monitored through ^{19}F-NMR spectroscopy (Figure 9). The ^{19}F-NMR spectra of [(F_2tmpa)Cu^{I}][$B(C_6F_5)_4$] displayed one signal at $\delta = -126.86$ ppm for the two fluorine atoms occupying the 3′-position of the two substituted pyridyl arms, and three signals at $\delta = -132.04$, −164.28, and −167.77 ppm for the fluorines of the $[B(C_6F_5)_4]^-$ counter anion. Upon dioxygen bubbling into the solution, the 3′-fluorine signal transformed into two new signals, one sharp peak at $\delta = -123.38$ ppm and another broad peak at −101.44 ppm, while the signals from $[B(C_6F_5)_4]^-$ remained unchanged. We assigned the former (i.e., $\delta = -123.38$ ppm) to the 3′-fluorine resonance of the diamagnetic μ-peroxo [(F_2tmpa)Cu^{II}–(O_2^{2-})–Cu^{II}(F_2tmpa)]$^{2+}$ species while the latter (i.e., $\delta = -101.44$ ppm) corresponded to the monomeric decomposition product, [(F_2tmpa)Cu^{II}(X)]$^{n+}$.

The dioxygen reactivity for [(MeTFE-tmpa)Cu^{I}][$B(C_6F_5)_4$] in THF-d_8 was also monitored through NMR spectroscopy (Figure 8). The ^{1}H-NMR spectrum of the copper(I) complex also showed four pyridyl proton signals between $\delta = 8.96$ and 7.20 ppm as well as two sharp resonances at $\delta = 4.73$ and $\delta = 2.17$ ppm corresponding to the methylene and methyl protons, respectively. Here, O_2 bubbling led to a spectral change similar to those observed for the copper(I) complexes of the parent TMPA and its electron-deficient derivative, F_2TMPA. The relatively sharp signals at $\delta = 11.19$ and 10.98 along with a series of resonances from 8.20 to 5.85 ppm originate from the μ-peroxo [(MeTFE-tmpa)Cu^{II}–(O_2^{2-})–Cu^{II}(MeTFE-tmpa)]$^{2+}$ complex which slowly decomposes over time, as observed from the gradual decrease in these signal intensities. The final decomposition product was again a paramagnetic monomer copper(II) species identified by signals at $\delta = 13.80$, 13.66, 12.52, 10.58, and 9.05 ppm along with resonances between 46.59 and 22.07 ppm in the paramagnetic region [35]. It is important to point out the presence of a more complicated ^{1}H-NMR pattern observed for the MeTFE-TMPA oxygenation reaction as compared to those observed for the TMPA or F_2TMPA analogue is possibly due to the lower symmetry of the cupric center or more significant separation of chemical shifts.

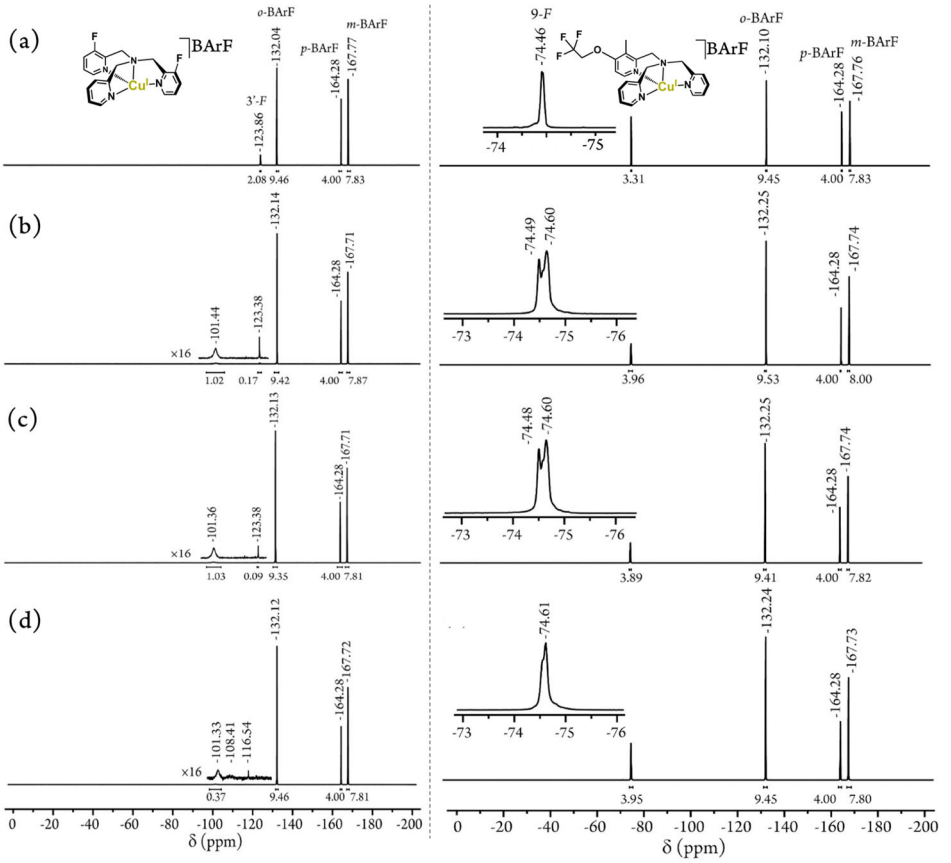

Figure 9. ^{19}F-NMR spectra of the oxygenation reaction of (left) [(F_2tmpa)Cu^{I}][$B(C_6F_5)_4$] and (right) [(MeTFE-tmpa)Cu^{I}][$B(C_6F_5)_4$] at (a) 0 min, (b) 1 min, (c) 15 min, and (d) 6 h in THF-d_8 (470 MHz) at room temperature. Peaks labeled as *o*-BArF, *p*-BArF, and *m*-BArF are for the *ortho*-, *para*-, and *meta*-fluorine atoms of the $[B(C_6F_5)_4]^-$ anion, respectively.

The ^{19}F-NMR spectra of the oxygenation of a THF-d_8 solution of [(MeTFE-tmpa)Cu^{I}][$B(C_6F_5)_4$] were also collected at room temperature (Figure 9). For the starting cuprous complex, the signal for the trifluoroethoxy (TFE) group appeared at δ = –74.46 ppm while the three fluorines of the $[B(C_6F_5)_4]^-$ anion were present in the more shielded, aromatic region. Upon dioxygen exposure, the TFE peak transformed into two new fluorine resonances at δ = –74.49 and –74.60 ppm. Over time, the signal at δ = –74.49 ppm gradually disappeared whereas the peak intensity at δ = –74.60 ppm increased. Therefore, the peak at δ = –74.49 ppm was assigned to the TFE-fluorines of the μ-peroxo [(MeTFE-tmpa)Cu^{II}–(O_2^{2-})–Cu^{II}(MeTFE-tmpa)]$^{2+}$ complex while the one at δ = –74.60 ppm corresponded to the TFE-fluorines of the final monomeric decomposition product. Here, the differences in ^{19}F-chemical shifts are significantly smaller as compared to those observed in the F_2TMPA analogue, possibly due to the fact that fluorine atoms are further removed from the copper center.

A qualitative comparison of the signal intensities of *trans*-peroxo-dicopper(II) species and the final cupric decomposition product, in both ^{1}H- and ^{19}F-NMR studies

(Figures 8 and 9), also support the findings concluded from the UV-vis experiments at room temperature (Figure 5), viz., that the *trans*-peroxo-dicopper(II) species bearing the more electron-rich MeTFE-TMPA chelate is more stable as compared to its more electron-deficient counterparts bearing either TMPA or F_2TMPA.

4. Conclusion

Tagging the two new, remotely substituted, TMPA-based chelates with fluorine and utilizing ^{19}F-NMR spectroscopy provided a useful means for probing the oxygenation reactions. This is particularly beneficial for antiferromagnetically coupled species such as the *trans*-peroxo dicopper(II) intermediate in which the sharpness and lack of extensive broadening of the NMR resonances result in their facile detection.

Our spectroscopic and electrochemical studies of the effects of variation in ligand electronic properties on the redox behavior and dioxygen reactivity of the corresponding copper(I) complexes support that ligand electron-donating ability can significantly affect the oxygenation reactions. The relative rates of formation of the 1:1 (i.e., *end-on* superoxo) and subsequent generation of the 2:1 (i.e., *trans*-peroxo) copper-O_2 intermediates are governed by temperature and ligand electronic effects. For both classes of the copper-dioxygen adducts, the main electronic transitions shift to lower energies as the electron-donating ability of the chelate diminishes. This change in the electronic character of the copper-O_2 core can be explained by stabilization of d_{z2} orbitals which is consistent with the increase in the reduction potentials.

Acknowledgement

We are thankful to Dr. Maxime A. Siegler for valuable discussions on X-ray crystallography. The Joint School of Nanoscience and Nanoengineering, a member of the National Nanotechnology Coordinated Infrastructure (NNCI), which is supported by the National Science Foundation (Grant ECCS-2025462), is acknowledged for providing access to the X-ray diffraction facility.

Disclosure statement

No potential conflict of interest was reported by the authors.

Funding

This material is based upon work supported by the National Science Foundation under Grant No. [2213341]. The authors are grateful to the University of North Carolina at Greensboro for the financial support provided in the form of startup funds, the Spartans ADVANCE Research Award, and the URSCO Undergraduate Research and Creativity Award (URCA).

ORCID

Runzi Li http://orcid.org/0000-0001-5016-2874
Firoz Shah Tuglak Khan http://orcid.org/0000-0002-3800-0423
Marcos Tapia http://orcid.org/0000-0002-6250-1711
Shabnam Hematian http://orcid.org/0000-0002-0788-7615

References

[1] R. Trammell, K. Rajabimoghadam, I. Garcia-Bosch. *Chem. Rev.*, **119**, 2954 (2019).
[2] E.I. Solomon, D.E. Heppner, E.M. Johnston, J.W. Ginsbach, J. Cirera, M. Qayyum, M.T. Kieber-Emmons, C.H. Kjaergaard, R.G. Hadt, L. Tian. *Chem. Rev.*, **114**, 3659 (2014).
[3] S.E. Allen, R.R. Walvoord, R. Padilla-Salinas, M.C. Kozlowski. *Chem. Rev.*, **113**, 6234 (2013).
[4] E.A. Lewis, W.B. Tolman. *Chem. Rev.*, **104**, 1047 (2004).
[5] K.D. Karlin, S. Kaderli, A.D. Zuberbühler. *Acc. Chem. Res.*, **30**, 139 (1997).
[6] D.A. Quist, D.E. Diaz, J.J. Liu, K.D. Karlin. *J. Biol. Inorg. Chem.*, **22**, 253 (2017).
[7] E.I. Solomon, J.W. Ginsbach, D.E. Heppner, M.T. Kieber-Emmons, C.H. Kjaergaard, P.J. Smeets, L. Tian, J.S. Woertink. *Faraday Discuss*, **148**, 11 (2011).
[8] J.P. Klinman. *Chem. Rev.*, **96**, 2541 (1996).
[9] R. Davydov, A.E. Herzog, R.J. Jodts, K.D. Karlin, B.M. Hoffman. *J Am Chem Soc*, **144**, 377 (2022).
[10] S.M. Adam, G.B. Wijeratne, P.J. Rogler, D.E. Diaz, D.A. Quist, J.J. Liu, K.D. Karlin. *Chem. Rev.*, **118**, 10840 (2018).
[11] C.E. Elwell, N.L. Gagnon, B.D. Neisen, D. Dhar, A.D. Spaeth, G.M. Yee, W.B. Tolman. *Chem. Rev.*, **117**, 2059 (2017).
[12] H.R. Lucas, L. Li, A.A.N. Sarjeant, M.A. Vance, E.I. Solomon, K.D. Karlin. *J. Am. Chem. Soc.*, **131**, 3230 (2009).
[13] L.M. Mirica, X. Ottenwaelder, T.D.P. Stack. *Chem. Rev*, **104**, 1013 (2004).
[14] K.D. Karlin, N. Wei, B. Jung, S. Kaderli, P. Niklaus, A.D. Zuberbuehler. *J. Am. Chem. Soc.*, **115**, 9506 (1993).
[15] M.J. Baldwin, P.K. Ross, J.E. Pate, Z. Tyeklar, K.D. Karlin, E.I. Solomon. *J. Am. Chem. Soc.*, **113**, 8671 (1991).
[16] K.D. Karlin, N. Wei, B. Jung, S. Kaderli, A.D. Zuberbuehler. *J. Am. Chem. Soc.*, **113**, 5868 (1991).
[17] R.R. Jacobson, Z. Tyeklar, A. Farooq, K.D. Karlin, S. Liu, J. Zubieta. *J. Am. Chem. Soc.*, **110**, 3690 (1988).
[18] S.Y. Quek, S. Debnath, S. Laxmi, M. van Gastel, T. Krämer, J. England. *J. Am. Chem. Soc.*, **143**, 19731 (2021).
[19] E.W. Dahl, H.T. Dong, N.K. Szymczak. *Chem. Commun. (Camb.)*, **54**, 892 (2018).
[20] S. Hematian, M.A. Siegler, K.D. Karlin. *J. Am. Chem. Soc.*, **134**, 18912 (2012).
[21] G.M. Sheldrick. *SHELXL-2018: Program for Crystal Structure Refinement*, University of GöTtingen, GöTtingen, Germany (2018).
[22] F.S.T. Khan, A.L. Waldbusser, M.C. Carrasco, H. Pourhadi, S. Hematian. *Dalton Trans.*, **50**, 7433 (2021).
[23] R. Li, F.S. Khan, S. Hematian. *Molecules*, **27**, 1000 (2022).
[24] C.X. Zhang, S. Kaderli, M. Costas, E-i Kim, Y.-M. Neuhold, K.D. Karlin, A.D. Zuberbühler. *Inorg. Chem.*, **42**, 1807 (2003).
[25] Z. Tyeklar, R.R. Jacobson, N. Wei, N.N. Murthy, J. Zubieta, K.D. Karlin. *J. Am. Chem. Soc.*, **115**, 2677 (1993).
[26] R.R. Jacobson, Z. Tyeklár, K.D. Karlin. *Inorg. Chim. Acta*, **181**, 111 (1991).
[27] T. Osako, K.D. Karlin, S. Itoh. *Inorg. Chem.*, **44**, 410 (2005).
[28] B. Lucchese, K.J. Humphreys, D.-H. Lee, C.D. Incarvito, R.D. Sommer, A.L. Rheingold, K.D. Karlin. *Inorg. Chem.*, **43**, 5987 (2004).
[29] D. Maiti, A.A. Narducci Sarjeant, S. Itoh, K.D. Karlin. *J. Am. Chem. Soc.*, **130**, 5644 (2008).
[30] B. Hathaway, G. Wilkinson, R. Gillard, J. McCleverty. Comprehensive Coordination Chemistry: *The Synthesis, Reactions, Properties and Applications of Coordination Compounds*, Pergamon Press, Oxford, Vol. **5**, pp. 533 (1987).
[31] A.W. Addison, T.N. Rao, J. Reedijk, J. van Rijn, G.C. Verschoor. *J. Chem. Soc. Dalton Trans.*, 1349 (1984). DOI:10.1039/DT9840001349
[32] N. Wei, N.N. Murthy, Q. Chen, J. Zubieta, K.D. Karlin. *Inorg. Chem.*, **33**, 1953 (1994).
[33] P.K. Ross, E.I. Solomon. *J. Am. Chem. Soc.*, **113**, 3246 (1991).
[34] E.I. Solomon. *Inorg. Chem.*, **55**, 6364 (2016).
[35] A. Nanthakumar, S. Fox, N.N. Murthy, K.D. Karlin. *J. Am. Chem. Soc.*, **119**, 3898 (1997).
[36] N.N. Murthy, K.D. Karlin, I. Bertini, C. Luchinat. *J. Am. Chem. Soc.*, **119**, 2156 (1997).